Journal of Innovative Optical Health Sciences
Vol. 4, No. 4 (2011) 385−393

DOI: 10.1142/S1793545811001691

World Scientific
www.worldscientific.com

PERFORMANCE OF BLIND DECONVOLUTION IN OPTOACOUSTIC TOMOGRAPHY

THOMAS JETZFELLNER and VASILIS NTZIACHRISTOS*
Institute for Biological and Medical Imaging
Technische Universität München and Helmholtz Center Munich
Ingolstaedter Landstr. 1, 85764 Neuherberg, Germany
**v.ntziachristos@tum.de*

Accepted 5 July 2011

In this paper, we consider the use of blind deconvolution for optoacoustic (photoacoustic) imaging and investigate the performance of the method as means for increasing the resolution of the reconstructed image beyond the physical restrictions of the system. The method is demonstrated with optoacoustic measurement obtained from six-day-old mice, imaged in the near-infrared using a broadband hydrophone in a circular scanning configuration. We find that estimates of the unknown point spread function, achieved by blind deconvolution, improve the resolution and contrast in the images and show promise for enhancing optoacoustic images.

Keywords: Optoacoustic; photoacoustic; tomography; multispectral; blind deconvolution; interpolated-model-matrix inversion (IMMI).

Optoacoustic tomography, also termed photoacoustic tomography, offers high-resolution mapping of intrinsic absorption and exogenous contrast agents in tissues.[1−6] Imaging is performed by illuminating the object or region of interest with short high-energy (1−100 mJ) laser pulses, thus creating an instantaneous temperature elevation and a corresponding local thermal expansion of tissue, at areas of light absorption. As a result, broadband ultrasonic waves are generated (typically in the 0.1−10 MHz range) that convey information on the local light energy deposition. Collecting tomographically the generated ultrasonic waves around the object and using optoacoustic inversion schemes, the source distribution can be reconstructed as an image representing local laser energy absorption within the object.

In contrast to conventional ultrasound imaging, attaining relatively low contrast between different soft tissues, optoacoustic tomography visualizes the optical contrast, which is significantly richer in distinguishing different tissues and biomarkers, including oxygenated and deoxygenated forms of hemoglobin or endogenously or extrinsically administered absorbers. Additionally, due to weak scattering of ultrasonic waves in biological tissues, the resolution is similar to that achieved with ultrasonography, i.e., it can reach 20−200 μm depending on the penetration depth and corresponding frequency spectrum used. By combining rich optical contrast with ultrasonic diffraction-limited resolution, optoacoustics holds a great promise to become the method of choice in a variety of small animal and clinical imaging applications.[7−9] Detection and

*Corresponding author.

visualization of spectrally distinct intrinsic tissue contrast and exogenous agents can be facilitated by acquiring optoacoustic data at multiple wavelengths and applying spectral processing and reconstruction algorithms.[10,11] By increasing the number of detection elements, it is also possible to build tomographic[12] and microscopic systems,[13,14] which are able to scan objects in real time. Real-time optoacoustic tomographs are able to provide direct insight into biological processes such as kidney perfusion[12] or cardiovascular dynamics.[15] Of particular interest is the development of multispectral optical tomography (MSOT),[10,16,17] which provides the capability to accurately resolve and quantify the volumetric biodistribution of molecular probes and tissue biomarkers. The method utilizes illumination at several wavelengths and this information is used to quantitatively resolve the spectra of various tissue molecules. An additional advantage of MSOT is that the separation of a molecular probe from background can be achieved in the absence of background measurements, i.e., there is no need to obtain data before probe administration.[17] This is useful for most molecular probes, which require some considerable time to deliver and localize at an intended target, typically 1 h or more. The information contained at multiple wavelengths is also employed to improve the accuracy of the reconstructed images as a function of depth and inhomogeneous light distribution.[17]

Despite advantages, the quality of optoacoustic images can be compromised by the convolution of the point-spread function (PSF) of the system with the underlying absorption image; a process typical of the imaging process. The PSF of a system can be generally experimentally measured by imaging an object of physical dimensions that are much smaller than the resolution of the imaging system. There are cases, where PSF is not provided for a system, even though there is a need to deconvolve the image to increase the quality of the reconstruction. Therefore we investigate the performance of blind deconvolution (BD) for optoacoustic tomography, which allows resolution improvements by at least partially improving on image "blurring"; typical of a convolution process. BD is a well-studied method in image processing and applied mathematics.[18–21] While in regular deconvolution the PSF is exactly measured and then used to recover the original image (unblur), BD estimates the PSF from the image or image set of interest. This method has already shown efficiency in medical imaging, for example in MRI,[22] SPECT[23] or ultrasound[24] images. It has been also considered in astronomy to improve images aquired by telescopes[25] or in microscopy to increase the image resolution beyond the limitations of the hardware.[26,27] In contrast to classical filtered back-projection algorithms,[28] which have in general an inferior signal-to-noise ratio (SNR) compared to IMMI,[29] we present the performance of BD on IMMI reconstructed *ex vivo* mouse images for optoacoustic data.

Generally in the field of image processing a blurred image g can be expressed as

$$g = h \otimes f, \tag{1}$$

where f is the original image, $\otimes$ is the convolution operator and h is a non-negative blur kernel of size that is small compared to the image size. Assuming the presence of a noise component n, Eq. (1) can be rewritten as

$$g = h \otimes f + n. \tag{2}$$

It is assumed that f and n are uncorrelated with covariance matrices M_f and M_n and that the additive noise is white, so $M_n = \sigma_n^2 I$ where I is the identity matrix. The challenge for BD is to estimate the unknown parameter h. To find this, a maximum likelihood estimate can be obtained.[30] The decomposition of image g is an ill-posed problem, because there exists an infinite number of solution pairs of h and f, which could give mathematically correct results. A unique solution may be obtained by making additional assumptions on the blur kernel.[30] For example, an estimate of the blur kernel can be used to reduce the result space. In our experiments we used an iterative algorithm, which was developed by Fish *et al.* and is discussed in detail in Ref. 31. Briefly the BD is based on the Lucy–Richardson (LR) deconvolution, which is itself an iterative algorithm. In each BD iteration, two LR deconvolution iterations are performed — one for an image evaluation and one for a PSF evaluation.[31] To stop the iterative BD algorithm, stop criteria must be introduced. In our case the iterative algorithms stops by under-running a certain error for two successively calculated iterations. The error is calculated by the root mean square (rms) error estimate for an entire image, which is defined by

$$rms = \sqrt{\frac{\int\int |f_{i-1} - f_i|^2 dxdy}{\int\int |f_{i-1}|^2 dxdy}}, \tag{3}$$

where f is the deconvolved image for a certain iteration i. The integration of Eq. (3) is performed over the entire image. Figure 1 depicts the performance of this approach using simulated images and 10 iteration steps. The initial PSF estimate was defined by a small matrix of 7×7, each element in the matrix having a value of one. Figure 1(a) depicts the original image, Fig. 1(b) the blurred

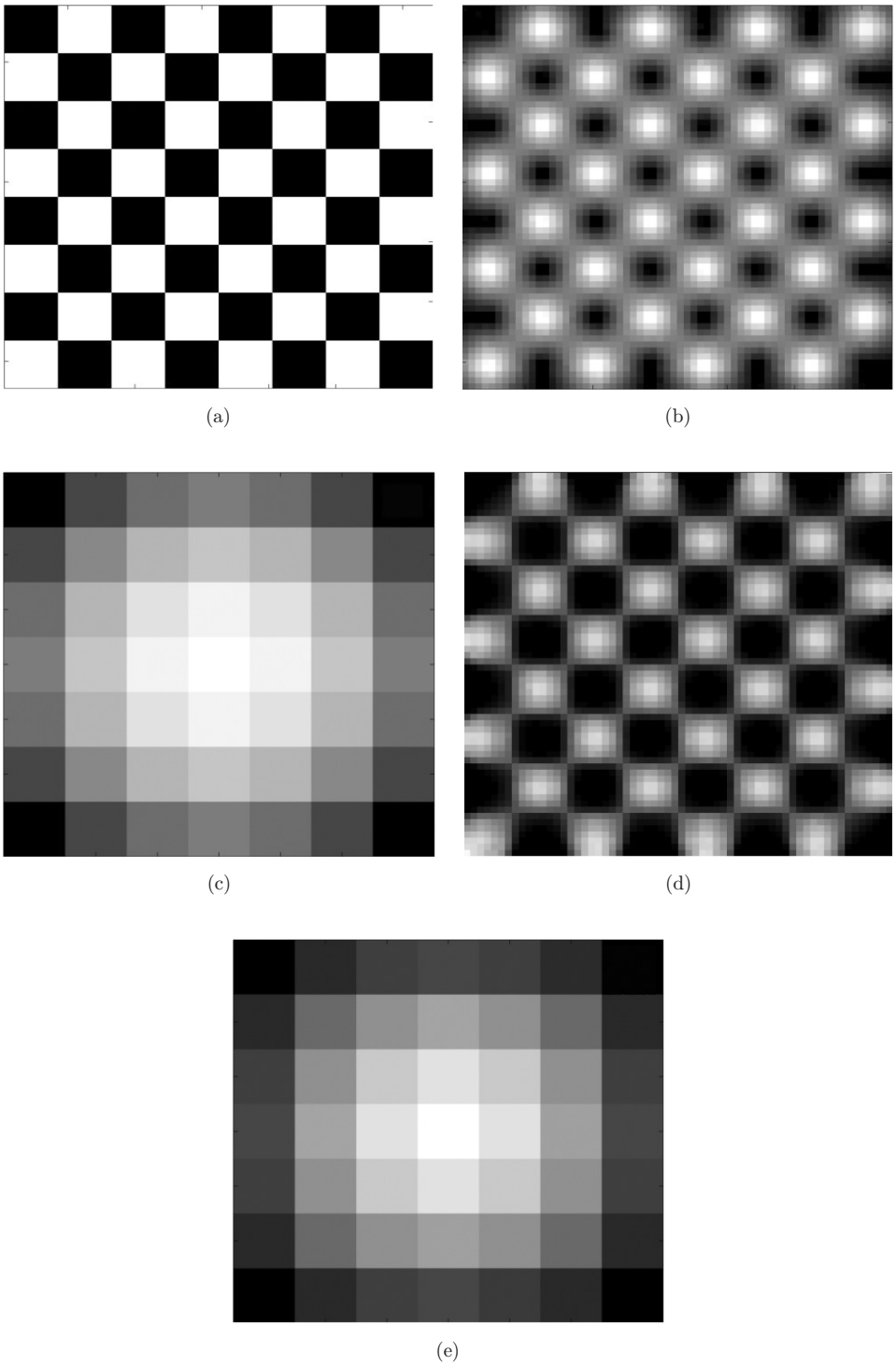

Fig. 1. (a) Undistorted image; (b) blurred image; (c) PSF which was used to get image (b); (d) recovered image after the blind deconvolution; and (e) recovered PSF.

image, Fig. 1(c) depicts the PSF assumed for the system, employed in image blurring (convolution), Fig. 1(d) shows the deconvolved image and Fig. 1(e) depicts the recovered PSF. As seen on Fig. 1(d), a marked resolution improvement is achieved after the application of BD, despite significant blurring of the image in Fig. 1(b).

To evaluate the performance of BD, we applied it to numerically simulated and experimentally acquired optoacoustic images, which were reconstructed by the recently published IMMI algorithm.[32] Assuming short laser pulses ($<1\,\mu$sec), the heat-confinement condition is fulfilled.[1] This means that the acoustic signal generated is proportional to the absorbed optical energy. Under this condition, and neglecting acoustic losses, the propagation equation for the acoustic fields is given by[33]:

$$\nabla^2 p(\vec{r},t) - \frac{1}{c_s^2}\frac{\partial^2}{\partial t^2}p(\vec{r},t) = \Gamma\frac{\partial H(r,t)}{\partial t}, \quad (4)$$

where c_s is the speed of sound in the medium, p is the pressure at time t at position r, Γ is the Grüneisen parameter, and H is the amount of energy absorbed in the tissue per unit volume and per unit time. In most practical cases, this equation can be directly inverted, i.e.[32,33]:

$$p(r,t) = \frac{\Gamma}{4\pi c}\frac{\partial}{\partial t}\int_{R=ct}\frac{H_r(r')}{R}dA', \quad (5)$$

where $R = r - r'$ and the integration is performed over a sphere with a radius of $R = ct$. In a two-dimensional (2D) geometry, for which all the sources lie in a plane, the integration can be performed over a circle. Then the unknown $H_r(r)$ distribution can be reconstructed by inversion of Eq. (5) and denotes the amount of photon absorption at each position r. The inversion can be performed using analytical solutions, such as back-projection algorithms, or model-based solutions that solve Eq. (5) numerically. In IMMI,[32,34] Eq. (5) is solved by applying linear interpolation to $H_r(r)$ and performing the integral analytically. This leads to a discretization of Eq. (5), given by the following matrix relation

$$p = \mathbf{M}z, \quad (6)$$

where p is a column vector representing the acoustic fields measured at a position (projection) r, for a set of times $\{t_i\}(i = 1,\ldots,I) : p_i = p(r,t_i)$; z is a column vector representing the values of the optoacoustic image on the grid $z_j = H(r_j)(j = 1,\ldots,J)$; and M is the acoustic forward-model matrix for a detector at r. Then, two common methods for inverting Eq. (6) are the Moore−Penrose pseudo-inverse[35] and the LSQR (least squares QR decomposition) algorithm.[36] The pseudo-inverse of $\mathbf{M}$ is given by

$$\mathbf{M}^+ = (\mathbf{M}^H\mathbf{M})^{-1}\mathbf{M}^H, \quad (7)$$

where $\mathbf{M}^H$ is the Hermitian transpose of $\mathbf{M}$. After the pseudo-inverse is calculated, the reconstructed optoacoustic image can then be readily obtained by:

$$z = \mathbf{M}^+ p. \quad (8)$$

The pseudo-inverse of a matrix corresponding to a given imaging system needs to be calculated only once; in this case the inversion can be performed fast, within milliseconds.

The second alternative considered, LSQR, is an iterative algorithm for solving linear equations.[36] Analytically, LSQR is identical to the conjugate gradient method. However, numerically LSQR was found to be more stable. LSQR is highly efficient when applied to sparse matrices. LSQR operations require that only the non-zero elements of the matrix are saved in memory, thus mitigating memory requirements. Since the model matrix $\mathbf{M}$ is sparse when the number of grid points (resolution) is high,[32] LSQR is an appropriate method for inverting Eq. (6).

In the next step we demonstrate the performance of BD for numerical simulated optoacoustic phantoms. In general an optoacoustic image $H_r(r)$ represents the total amount of optical energy transferred to the imaged object from a single light pulse at a point r, which can be described by

$$H(r) = \mu_a(r)U(r), \quad (9)$$

where $\mu_a(r)$ is the absorption coefficient and $U(r)$ is the light fluence. To model the light fluence for our experiments, we assumed diffusion approximation to light transport equation,[37] i.e.,

$$-\nabla D(\vec{r})\nabla U(\vec{r}) + \mu_a(\vec{r})U(\vec{r}) = q_0, \quad (10)$$

where $D = 1/[3(\mu_s' + \mu_a)]$ is the spatially dependent diffusion coefficient of the medium, U is the light intensity, μ_a is the optical absorption coefficient, μ_s' is the reduced scattering coefficient and q_0 is the source term. When the exterior medium is non-scattering, the behavior of $U(r)$ on the interface is

given by the Robin boundary condition[38]:

$$U(\vec{r}) + 2D(\vec{r})\hat{\mathbf{n}} \cdot \nabla \cdot U(\vec{r}) = 0, \quad \vec{r} \in \partial\Omega, \qquad (11)$$

where $\partial\Omega$ is the boundary of the object and $\hat{\mathbf{n}}$ is a unit vector normal to $\partial\Omega$ and pointing outward. Clearly, for heterogeneous media, solutions for Eq. (10) can only be obtained numerically. In our work, we used a finite volume method (FVM) solution approach.[39] After computing the optoacoustic source distribution with Eq. (9), we simulated the optoacoustic signals by using Eqs. (5) and (6).

All the algorithms were implemented in Matlab (Mathworks Inc., Natick, MA, USA), and executed on an Intel® Core™2 Quad Processor CPU operating at 2.67 GHz with 4 Gb of RAM. All the model-based reconstructions were obtained using LSQR for inversion.

We numerically tested the performance for a round tissue-mimicking phantom containing several inclusions with higher absorption compared to the background. To the bulk of the phantom was assigned an absorption coefficient of $\mu_a = 0.2\,\mathrm{cm}^{-1}$, whereas the insertions had absorption coefficients of $2\,\mathrm{cm}^{-1}$. The scattering coefficient was chosen to be constant and had the value of $10\,\mathrm{cm}^{-1}$. We computed the simulated acoustic signals by using the forward solution of IMMI, assuming constant and uniform surface illumination and circular detection geometry with 360 projections. To reconstruct the numerical phantom signals we used IMMI for 180 projections (Fig. 2(a)). Figure 2(b) shows the blurred version of Fig. 2(a), where the PSF of Fig. 2(c) was used.[40] As stop criteria we defined a maximum allowed error of 5.0e-004, which was reached after 18 iterations. As expected, BD improved the optoacoustic image (marked by arrows) and shown in Fig. 2(d) and gave a good estimation for the PSF we used to distort the image.

For the investigation of the performance of BD on experimental data, we employed a first-generation single detector MSOT system described in detail in Ref. 41. In brief, the experimental setup employed (Fig. 3) rotates the object of interest in front of a 7.5 MHz ultrasonic transducer (Model V320, Panametrics-NDT, Waltham, MA, USA) to obtain 360° tomographic scans of the generated optoacoustic response. The excitation wavelength employed for the measurements herein was 650 nm, obtained from a nanosecond Optical Parametric Oscillator (OPO) Spectra Physics laser. Measurements from the heads of six-day-old mice were captured post-mortem at three-degree steps. In order to improve SNR of the signals, each projection was obtained by averaging 32 independent measurements, resulting in $32 \times 120 = 3840$ measurements which were acquired in approximately 10 min. The model matrix, which was subsequently inverted, consisted of $90{,}000 \times 381{,}900$ elements corresponding to a reconstructed image of 300×300 pixels, of approximately 64-micron resolution. Figure 4(a) shows the reconstructed image by IMMI and Fig. 4(b) the result of the BD. Despite the complexity of the images, compared to the sample

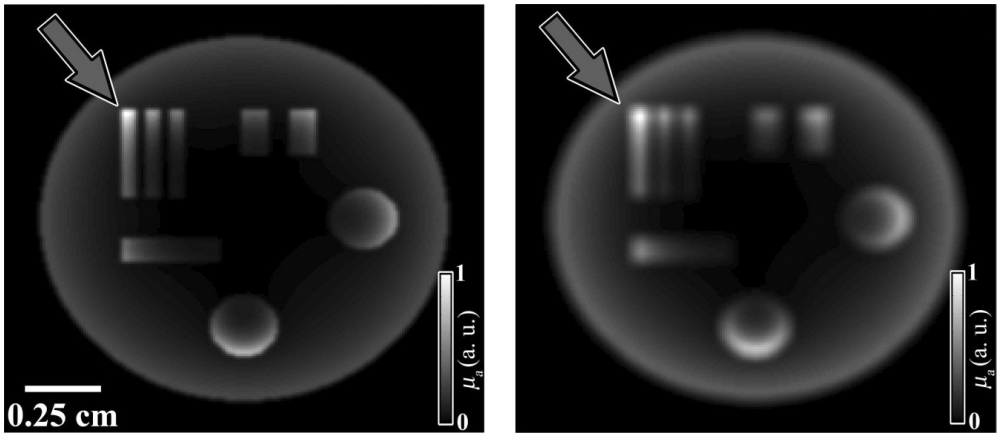

(a) (b)

Fig. 2. (a) Unblurred optoacoustic image; (b) blurred optoacoustic image; (c) PSF used to blur image (a); (d) recovered image using BD; and (e) recovered PSF.

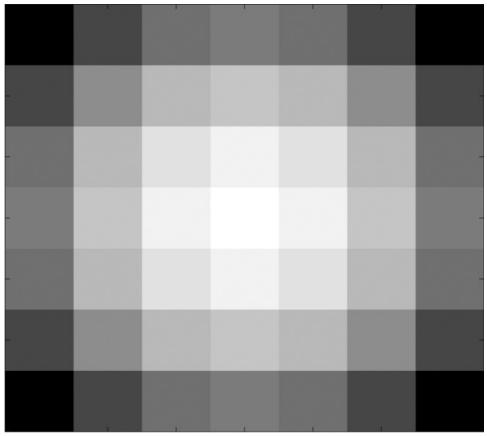

(c)

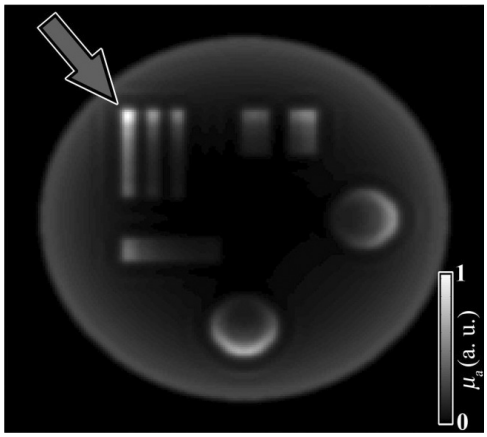

(d)

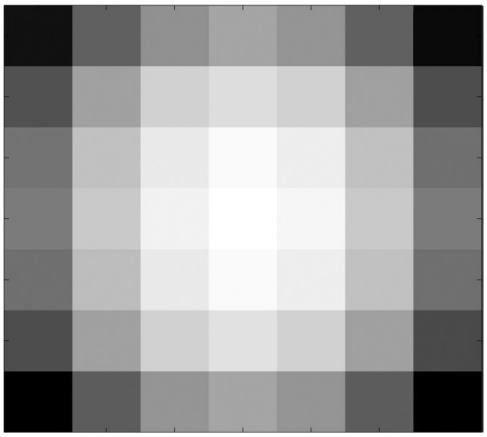

(e)

Fig. 2. (*Continued*)

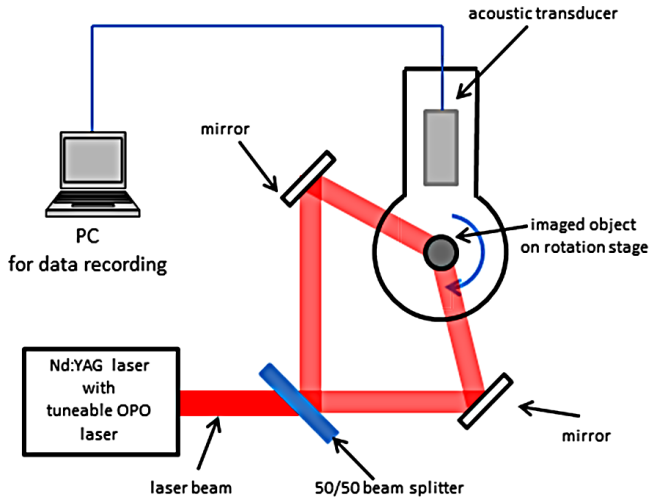

Fig. 3. Sketch of the optoacoustic setup used.

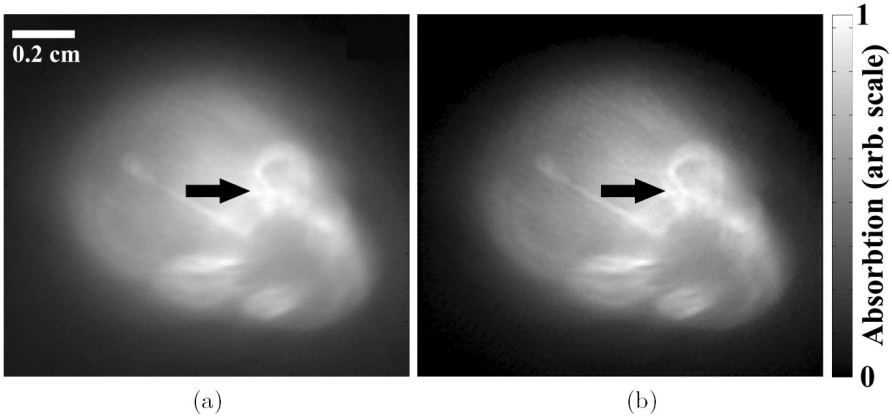

Fig. 4. (a) IMMI reconstructed mouse head; and (b) result after applying blind deconvolution.

images in Figs. 1 and 2, the deconvolved image depicts an improvement, manifested as sharpness and corresponding contrast betterment. This is shown in detail for both images for the region marked with an arrow. Here we can see in the uncorrected image that the absorbing structure close to the eye socket is blurry and the borders are not well defined. However, in the deconvolved image the blurring is reduced and the structure is better defined.

BD for experimental data has generally a lower performance compared to simulated data, which is related to the spatial dependency of the PSF of acoustic detectors. In our experiments we assumed an invariant PSF for the optoacoustic image. This is true as long as the measured object is small enough to stay in the focus of the transducer, because there the spatial dependency of the PSF is minimal.[42,43] Nevertheless we have shown the application of BD in IMMI-reconstructed optoacoustic images,[32] demonstrated on simulated phantoms and experimental datasets from the mouse head. The method increased the resolution of the optoacoustic image, subjectively evaluated by image observation. This is achieved by using an iterative BD algorithm, which estimates the PSF of an optoacoustic system. For a successful application of the method it is important to have good quality images, i.e., images that preserve as best as possible spatial frequency components and contain as few artifacts as possible. Such necessary image quality was provided herein by the recently published IMMI inversion method.[32] Conversely, traditional inversion schemes, such as back-projection, introduce many artifacts in the reconstructed image,[29] so the blur kernel cannot be sufficiently estimated. In this study we used a straightforward implementation of the BD algorithm, so it still holds potential for optimizations. BD can be useful in different implementations of optoacoustic imaging, including mesoscopy and microscopy

References

1. R. A. Kruger, "Photoacoustic ultrasound (PAUS) — Reconstruction tomography," *Med. Phys.* **22**, 1605 (1995).
2. X. Wang, Y. Pang, G. Ku, X. Xie, G. Stoica, L. V. Wang, "Noninvasive laser-induced photoacoustic tomography for structural and functional *in vivo* imaging of the brain," *Nat. Biotechnol.* **21**, 803−806 (2003).
3. D. Razansky, V. Ntziachristos, "Hybrid photoacoustic fluorescence molecular tomography using finite-element-based inversion," *Med. Phys.* **34**, 4293 (2007).
4. R. A. Kruger, W. L. Kiser Jr, D. R. Reinecke, G. A. Kruger, K. D. Miller, "Thermoacoustic optical molecular imaging of small animals," *Mol. Imag.* **2**, 113−123 (2003).
5. B. Z. Yin, D. Xing, Y. Wang, Y. G. Zeng, Y. G. Zeng, Y. Tan, Q. Chen, "Fast photoacoustic imaging system based on 320-element linear transducer array," *Phys. Med. Biol.* **49**, 1339−1346 (2004).
6. D. W. Yang, D. Xing, H. M. Gu, Y. Tan, L. M. Zeng, "Fast multielement phase-controlled photoacoustic imaging based on limited-field-filtered back-projection algorithm," *Appl. Phys. Lett.* **87**, 194101 (2005).
7. V. Ntziachristos, D. Razansky, "Molecular imaging by means of multispectral optoacoustic tomography (MSOT)," *Chem. Rev.* **110**(5), 2783−2794 (2010).
8. S. H. Yang, D. Xing, Y. Q. Lao, D. W. Yang, L. M. Zeng, L. Z. Xiang, W. R. Chen, "Noninvasive monitoring of traumatic brain injury and post-traumatic rehabilitation with laser-induced photoacoustic

imaging," *Appl. Phys. Lett.* **90**, 243902-1−243902-3 (2007).
9. D. W. Yang, D. Xing, S. H. Yang, L. Z. Xiang, "Fast full-view photoacoustic imaging by combined scanning with a linear transducer array," *Opt. Exp.* **15**, 15566−15575 (2007).
10. D. Razansky, C. Vinegoni, V. Ntziachristos, "Multispectral photoacoustic imaging of fluorochromes in small animals," *Opt. Lett.* **32**, 2891 (2007).
11. R. I. Siphanto, K. K. Thumma, R. G. M. Kolkman, T. G. van Leeuwen, F. F. M. de Mul, J. W. van Neck, L. N. A. van Adrichem, W. Steenbergen, "Serial noninvasive photoacoustic imaging of neovascularization in tumor angiogenesis," *Opt. Exp.* **13**, 89 (2005).
12. A. Buehler, E. Herzog, D. Razansky, V. Ntziachristos, "Video rate optoacoustic tomography of mouse kidney perfusion," *Opt. Lett.* **35**, 2475−2477 (2010).
13. L. Song, K. Maslov, L. V. Wang, "Section-illumination photoacoustic microscopy for dynamic 3D imaging of microcirculation *in vivo*," *Opt. Lett.* **35**, 1482−1484 (2010).
14. R. J. Zemp, L. A. Song, R. Bitton, K. K. Shung, L. H. V. Wang, "Real time photoacoustic microscopy *in vivo* with a 30-MHz ultrasound array transducer," *Opt. Exp.* **16**, 7915−7928 (2008).
15. A. Taruttis, E. Herzog, D. Razansky, V. Ntziachristos, "Real-time imaging of cardiovascular dynamics and circulating gold nanorods with multispectral optoacoustic tomography," *Opt. Exp.* **18**, 19,592−19,602 (2010).
16. D. Razansky, C. Vinegoni, V. Ntziachristos, "Mesoscopic imaging of fluorescent proteins using multispectral optoacoustic tomography (MSOT)," San Jose, CA, USA, 2009, 71770D-71770D-6.
17. V. Ntziachristos, D. Razansky, "Molecular imaging by means of multispectral optoacoustic tomography (MSOT)," *Chem. Rev.* **110**, 2783−2794 (2010).
18. G. R. Ayers, J. C. Dainty, "Iterative blind deconvolution method and its applications," *Opt. Lett.* **13**, 547−549 (1988).
19. E. Thiébaut, J. M. Conan, "Strict *a priori* constraints for maximum-likelihood blind deconvolution," *J. Opt. Soc. Am. A* **12**, 485−492 (1995).
20. A. C. Likas, N. P. Galatsanos, "A variational approach for Bayesian blind image deconvolution," *IEEE Transactions on Signal Processing* **52**, 2222−2233 (2004).
21. R. Molina, A. K. Katsaggelos, J. Abad, J. Mateos, "A Bayesian approach to blind deconvolution based on Dirichlet distributions," in *IEEE International Conference on Acoustics, Speech, and Signal Processing, 1997. ICASS* P-97, 1997, Vol. 4, pp. 2809−2812 (1997).
22. A. S. Carasso, "Direct blind deconvolution," *SIAM J. Appl. Math.* **61**, 1980−2007 (2001).
23. M. Mignotte, J. Meunier, "Three-dimensional blind deconvolution of SPECT images," *IEEE Transactions on Biomedical Engineering* **47**, 274−280 (2000).
24. T. Taxt, J. Strand, "Two-dimensional noise-robust blind deconvolution of ultrasound images," *IEEE Transactions on Ultrasonics, Ferroelectrics and Frequency Control* **48**, 861−866 (2001).
25. P. Barmby, D. E. McLaughlin, W. E. Harris, G. L. H. Harris, D. A. Forbes, "Structural parameters for globular clusters in M31 and generalizations for the fundamental plane," *Astro. J.* **133**, 2764−2786 (2007).
26. F. Sroubek, G. Cristobal, J. Flusser, "A unified approach to super-resolution and multichannel blind deconvolution," *IEEE Transactions on Image Processing* **16**, 2322−2332 (2007).
27. J. B. Sibarita, "Deconvolution microscopy," *Adv. Biochem. Eng. Biotechnol.* **95**, 201−243 (2005).
28. L. M. Zeng, D. Xing, H. M. Gu, D. W. Yang, S. H. Yang, L. Z. Xiang, "High antinoise photoacoustic tomography based on a modified filtered backprojection algorithm with combination wavelet," *Med. Phys.* **34**, 556−563 (2007).
29. T. Jetzfellner, A. Rosenthal, K. H. Englmeier, A. Dima, M. Á. Araque Caballero, D. Razansky, V. Ntziachristos, "Interpolated model-matrix optoacoustic tomography of the mouse brain," *Appl. Phys. Lett.* **98** (2011).
30. D. Kundur, D. Hatzinakos, "Blind image deconvolution revisited," *IEEE Signal Proc. Magazine* **13**, 61−63 (1996).
31. D. A. Fish, A. M. Brinicombe, E. R. Pike, J. G. Walker, "Blind deconvolution by means of the Richardson−Lucy algorithm," *J. Opt. Soc. Amer. A* **12**, 58−65 (1995).
32. A. Rosenthal, D. Razansky, V. Ntziachristos, "Fast semi-analytical model-based acoustic inversion for quantitative optoacoustic tomography," *IEEE Transactions on Medical Imaging* **29**, 1275−1285 (2010).
33. B. T. Cox, S. Kara, S. R. Arridge, P. C. Beard, "k-Space propagation models for acoustically heterogeneous media: Application to biomedical photoacoustics," *J. Acoust. Soc. Amer.* **121**, 3453 (2007).
34. T. Jetzfellner, A. Rosenthal, A. Buehler, A. Dima, K. H. Englmeier, V. Ntziachristos, D. Razansky, "Optoacoustic tomography with varying illumination and non-uniform detection patterns," *J. Opt. Soc. Amer. A Opt. Image. Sci. Vis.* **27**, 2488−2495 (2010).

35. G. Golub, *Matrix Computations*, Johns Hopkins University Press, Baltimore, 3rd edn. (1996).
36. C. C. Paige, M. A. Saunders, "LSQR: An algorithm for sparse linear equations and sparse least squares," *ACM Trans. Math. Software* **8**, 43−71 (1982).
37. T. Jetzfellner, D. Razansky, A. Rosenthal, R. Schulz, K. Englmeier, V. Ntziachristos, "Performance of iterative optoacoustic tomography with experimental data," *Appl. Phys. Lett.* **95**, 013703 (2009).
38. M. Schweiger, S. R. Arridge, M. Hiraoka, D. T. Delpy, "The finite element method for the propagation of light in scattering media: Boundary and source conditions," *Med. Phys.* **22**, 1779−1792 (1995).
39. W. Bangerth, R. Hartmann, G. Kanschat, "Deal. II — A general-purpose object-oriented finite element library," *ACM Transact. Math. Software* **33**, 24/1−24/27 (2007).
40. M. Xu, L. V. Wang, "Universal back-projection algorithm for photoacoustic computed tomography," *Phys. Rev. E* **71**, 016706 (2005).
41. R. Ma, A. Taruttis, V. Ntziachristos, D. Razansky, "Multispectral optoacoustic tomography (MSOT) scanner for whole-body small animal imaging," *Opt. Exp.* **17**, 21,414−21,426 (2009).
42. A. Rosenthal, V. Ntziachristos, D. Razansky, "Optoacoustic methods for frequency calibration of ultrasonic sensors," *IEEE Trans. Ultrasonics, Ferroelectrics and Frequency Control* **58**, 316−326 (2011).
43. A. Rosenthal, V. Ntziachristos, D. Razansky, "Model-based optoacoustic inversion with arbitrary-shape detectors," *Med. Phys.* **38**(7), 4285−4295 (2011).